Journal of The Electrochemical Society, **147** (12) 4485-4493 (2000)
S0013-4651(00)08-104-0 CCC: $7.00 © The Electrochemical Society, Inc.

Computational Fluid Dynamics Modeling of Proton Exchange Membrane Fuel Cells

Sukkee Um,[a] C.-Y. Wang,[a,*,z] and K. S. Chen[b,*]

[a]*GATE Center for Advanced Energy Storage, Department of Mechanical and Nuclear Engineering, The Pennsylvania State University, University Park, Pennsylvania 16802, USA*
[b]*Engineering Sciences Center, Sandia National Laboratories, Albuquerque, New Mexico 87185-0834, USA*

A transient, multidimensional model has been developed to simulate proton exchange membrane fuel cells. The model accounts simultaneously for electrochemical kinetics, current distribution, hydrodynamics, and multicomponent transport. A single set of conservation equations valid for flow channels, gas-diffusion electrodes, catalyst layers, and the membrane region are developed and numerically solved using a finite-volume-based computational fluid dynamics technique. The numerical model is validated against published experimental data with good agreement. Subsequently, the model is applied to explore hydrogen dilution effects in the anode feed. The predicted polarization curves under hydrogen dilution conditions are in qualitative agreement with recent experiments reported in the literature. The detailed two-dimensional electrochemical and flow/transport simulations further reveal that in the presence of hydrogen dilution in the fuel stream, hydrogen is depleted at the reaction surface, resulting in substantial anode mass transport polarization and hence a lower current density that is limited by hydrogen transport from the fuel stream to the reaction site. Finally, a transient simulation of the cell current density response to a step change in cell voltage is reported.

Manuscript submitted August 22, 2000; revised manuscript received August 27, 2000.

Proton exchange membrane fuel cell (PEMFC) engines can potentially replace the internal combustion engine for transportation because they are clean, quiet, energy efficient, modular, and capable of quick start-up. Since a PEMFC simultaneously involves electrochemical reactions, current distribution, hydrodynamics, multicomponent transport, and heat transfer, a comprehensive mathematical model is needed to gain a fundamental understanding of the interacting electrochemical and transport phenomena and to provide a computer-aided tool for design and optimization of future fuel cell engines.

Performance of a fuel cell is measured by its current-voltage relation (*i.e.,* the polarization curve). At a particular current, the voltage drop is mainly caused by (*i*) overpotentials of electrochemical reactions (mainly on the cathode), (*ii*) the ohmic drop across the ionomeric membrane, and (*iii*) the mass transport limitations of reactants and products. At high current densities of special interest to vehicular applications, excessive water is produced within the air cathode in the form of liquid, thus leading to a gas-liquid two-phase flow in the porous electrode. The ensuing two-phase transport of gaseous reactants to the reaction surface, *i.e.,* the cathode/membrane interface, becomes a limiting mechanism for cell performance, particularly at high current densities (*e.g.,* >1 A/cm^2). On the anode side, when reformate is used for the feed gas, the incoming hydrogen stream is diluted with nitrogen and carbon dioxide. The effects of hydrogen dilution on anode performance, particularly under high fuel utilization conditions, are significant.[1,2]

Excellent reviews of hydrogen PEMFC research up to the mid-1990s were presented by Prater[3] and Gottesfeld.[4] Modeling and computer simulation of hydrogen fuel cells have been attempted by a number of groups with the common goal of better understanding and hence optimizing fuel cell systems. Notable work includes that of Bernardi and Verbrugge[5,6] and Springer *et al.*[7,8] whose models are essentially one dimensional. Fuller and Newman,[9] Nguyen and White,[10] Garau *et al.*,[11] and Yi and Nguyen[12,13] developed pseudo two-dimensional models accounting for composition changes along the flow path. While such models are useful for small single cells, their applicability to large-scale fuel cells, particularly under high fuel utilization conditions, is limited. Nevertheless, the one-dimensional models of Bernardi and Verbrugge[5,6] and Springer *et al.*[7,8] provided a fundamental framework to build multidimensional models that followed. The pseudo two-dimensional models developed by Fuller and Newman,[9] Nguyen and White,[10] and later Yi and Nguyen[12] further demonstrated the important roles played by water and heat management in maintaining high performance of PEMFCs.

Most recently, Gurau *et al.*[11] presented a two-dimensional model of transport phenomena in PEM fuel cells. This work illustrated the utility of a multidimensional model in the understanding of the internal conditions of a fuel cell such as the oxygen and water distributions. In a separate development, Yi and Nguyen[13] formulated a two-dimensional model to explore hydrodynamics and multicomponent transport in the air cathode of PEMFCs with an interdigitated flow field. Recent efforts have also been made to model two-phase flow and transport in the air cathode, a critical issue that has repeatedly been emphasized in the literature for fuel cells operated under high current densities.[14,15]

The objective of this study is two-fold. One goal is to develop a transient, multidimensional model for electrochemical kinetics, current distribution, fuel and oxidant flow, and multicomponent transport in a realistic fuel cell based on a finite-volume-based computational fluid dynamics (CFD) approach. The CFD method was first adapted to electrochemical systems by Gu *et al.*[16] and has since been applied successfully to a variety of battery systems including lead-acid, nickel-cadmium, nickel-metal hydride, lithium-ion, and the primary Li/$SOCl_2$ cell.[16-22] The work here is intended to extend the efficient single-domain CFD formulation previously developed for batteries to PEMFCs. The second goal, and one of practical importance, is to explore hydrogen dilution effects on PEMFCs running on reformate gas. Such effects were most recently investigated experimentally but have not been modeled.

The following section describes a transient, multidimensional mathematical model for electrochemical and transport processes occurring inside a PEMFC. Model validation against the experimental data of Ticianelli *et al.*[23] is presented in the Results and Discussion section along with a detailed, two-dimensional study of hydrogen dilution effects. The last section summarizes the major conclusions from this study and identifies further research based on the present CFD modeling framework.

Numerical Model

Figure 1 schematically shows a PEMFC fuel cell divided into seven subregions: the anode gas channel, gas-diffusion anode, anode catalyst layer, ionomeric membrane, cathode catalyst layer, gas-diffusion cathode, and cathode flow channel. Distinct from previous models, the present model considers the anode feed consisting of hydrogen, water vapor, and nitrogen to simulate reformate gas, whereas humidified air is fed into the cathode channel. Hydrogen

* Electrochemical Society Active Member.
z E-mail: cxw31@psu.edu

S0013-4651(00)08-104-0 CCC: $7.00

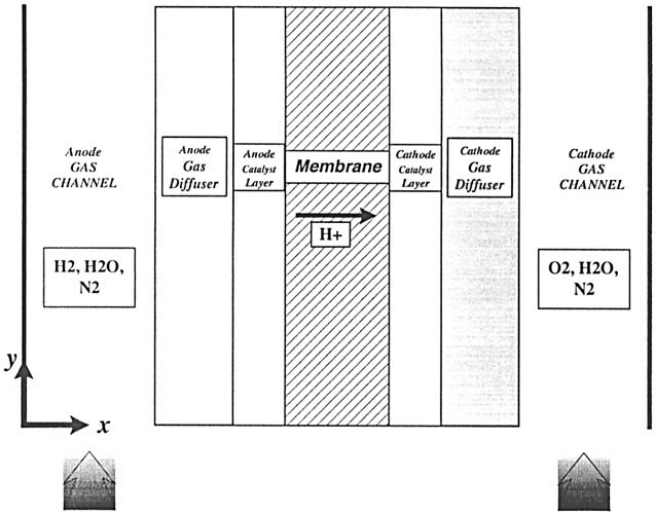

Figure 1. Schematic diagram of a proton exchange membrane fuel cell (PEMFC).

oxidation and oxygen reduction reactions are considered to occur only within the active catalyst layers where Pt/C catalysts are intermixed uniformly with recast ionomer. Other aspects of hydrogen fuel cell modeling can be found in the works of Bernardi and Verbrugge[6] and Springer *et al.*[8]

The fuel and oxidant flow rates can be described by a stoichiometric flow ratio, ζ, defined as the amount of reactant in the chamber gas feed divided by the amount required by the electrochemical reaction. That is

$$\zeta_+ = X^0_{O_2}\vartheta^0_+\frac{p_+}{RT}\frac{4F}{IA} \quad [1]$$

$$\zeta_- = X^0_{H_2}\vartheta^0_-\frac{p_-}{RT}\frac{2F}{IA} \quad [2]$$

where ϑ^0 is the inlet volumetric flow rate to a gas channel, p and T the pressure and temperature, R and F the universal gas constant and Faraday's constant, I the current density, and A the electrode surface area. The subscripts (+) and (−) denote the cathode and anode sides, respectively. For convenience, the stoichiometric flow ratios defined in Eq. 1 and 2 are based on the reference current density of 1 A/cm^2 here so that the ratios can also be considered as dimensionless flow rates of the fuel and oxidant.

Model assumptions.—This model assumes (*i*) ideal gas mixtures; (*ii*) incompressible and laminar flow due to small pressure gradients and flow velocities; (*iii*) isotropic and homogeneous electrodes, catalyst layers, and membrane; (*iv*) constant cell temperature; and (*v*) negligible ohmic potential drop in the electronically conductive solid matrix of porous electrodes and catalyst layers as well as the current collectors.

Governing equations.—In contrast to the approach of Gurau *et al.*,[11] which employs separate differential equations for different subregions, we take the single-domain approach used in our previous battery models in which a single set of governing equations valid for all subregions is used. As a result, no interfacial conditions are required to be specified at internal boundaries between various regions. Generally, fuel cell operation under isothermal conditions is described by mass, momentum, species, and charge conservation principles. Thus, under the above-mentioned assumptions, the model equations can be written, in vector form, as[19]

$$\frac{\partial(\rho\epsilon)}{\partial t} + \nabla\cdot(\epsilon\rho\mathbf{u}) = 0 \quad [3]$$

$$\frac{\partial(\rho\epsilon\mathbf{u})}{\partial t} + \nabla\cdot(\epsilon\rho\mathbf{u}\mathbf{u}) = -\epsilon\nabla p + \nabla\cdot(\epsilon\mu^{\text{eff}}\nabla\mathbf{u}) + S_u \quad [4]$$

$$\frac{\partial(\epsilon X_k)}{\partial t} + \nabla\cdot(\epsilon\mathbf{u}X_k) = \nabla\cdot(D_k^{\text{eff}}\nabla X_k) + S_k \quad [5]$$

$$\nabla\cdot(\sigma_e^{\text{eff}}\nabla\Phi_e) + S_\Phi = 0 \quad [6]$$

Here, $\mathbf{u}$, p, X_k, and Φ_e denote the intrinsic fluid velocity vector, pressure, mole fraction of chemical species k, and the phase potential of the electrolyte membrane, respectively. The diffusion coefficient of species k and ionic conductivity of the membrane phase in Eq. 5 and 6 are effective values modified via Bruggman correlation to account for the effects of porosity and tortuosity in porous electrodes, catalyst layers, and the membrane. That is

$$D_k^{\text{eff}} = \epsilon_m^{1.5}D_k \quad [7]$$

$$\sigma_k^{\text{eff}} = \epsilon_m^{1.5}\sigma_k \quad [8]$$

where ϵ_m is the volume fraction of the membrane phase. Other symbols in Eq. 3 through 8 can be found in the List of Symbols.

It is worth further explaining the mole fraction of oxygen appearing in Eq. 5 because oxygen is a gaseous species in the cathode flow channel and gas-diffusion electrode but becomes a species dissolved in the electrolyte in the catalyst layer and membrane regions. Our definition is given by

$$X_k = \begin{cases} c_k^g/c_{\text{tot}} & \text{in the gas phase} \\ c_k^e/c_{\text{tot}} & \text{in the electrolyte} \end{cases} \quad [9]$$

where c_k is the molar concentration of species k and superscripts g and e denote the gas and the electrolyte phases, respectively. Thus, X_k is a true mole fraction in the gas phase but is a pseudo mole fraction when species k is in the dissolved form. In addition, there is a discontinuity in the value of X_k at the interface between the gas-diffusion electrode and the catalyst layer due to the following thermodynamic relation

$$c_k^{e,\text{sat}} = \frac{RT}{H}c_k^g = H'c_k^g \quad [10]$$

where H is the Henry's law constant equal to 2×10^5 atm cm^3/mol for oxygen in the membrane.[5] The dimensionless Henry's constant, H', is thus approximately equal to 0.15 at 80°C.

In spite of the discontinuity in X_k across the interface between the catalyst layer and gas-diffusion electrode, the single-domain formulation, Eq. 5, intrinsically maintains the balance of species fluxes; namely

$$-(D_k^{\text{eff}})_-\left.\frac{\partial X_k}{\partial n}\right|_- = -(D_k^{\text{eff}})_+\left.\frac{\partial X_k}{\partial n}\right|_+ \quad [11]$$

where the symbols (−) and (+) stand for the left and right sides of the interface. Substituting the definition of X_k given in Eq. 9 into Eq. 11 yields the following interfacial balance of species fluxes

$$-D_e^{\text{eff}}\left.\frac{\partial c_k^e}{\partial n}\right|_- = -D_g^{\text{eff}}\left.\frac{\partial c_k^g}{\partial n}\right|_+ \quad [12]$$

Notice also that three source terms, S_u, S_k, and S_Φ, appear in momentum, species, and charge conservation equations to represent various volumetric sources or sinks arising from each subregion of a fuel cell. Detailed expressions of these source terms are given in Table I. Specifically, the momentum source term is used to describe Darcy's drag for flow through porous electrodes, active catalyst layers, and the membrane.[6,11,16] If there is very small hydraulic permeability (*e.g.*, 10^{-14} cm^2) in the membrane region, the pore velocity becomes so small that the inertia and viscous terms in Eq. 4 drop off, and the momentum equation reduces to the well-known Darcy's law as used by Bernardi and Verbrugge.[6] In addition, electro-osmotic drag arising from the catalyst layers and the membrane is also included.

Either generation or consumption of chemical species k and the creation of electric current (see Table I) occurs only in the active cat-

S0013-4651(00)08-104-0 CCC: $7.00

Table I. Source terms for momentum, species, and charge conservation equations in various regions.

	S_u	S_k	S_Φ
Gas channels	0	0	N/A
Backing layers	$-\frac{\mu}{K}\epsilon^2\mathbf{u}$	0	0
Catalyst Layers	$-\frac{\mu}{k_p}\epsilon_m\epsilon_{mc}\mathbf{u} + \frac{k_\Phi}{k_p}z_f c_f F\nabla\Phi_e$	$-\frac{j_a}{2Fc_{tota}}$ for H_2 $\frac{j_c}{4Fc_{totc}}$ for O_2 $-\frac{j_c}{2Fc_{totc}}$ for H_2O	j
Membrane	$-\frac{\mu}{k_p}\epsilon_m\mathbf{u} + \frac{k_\Phi}{k_p}z_f c_f F\nabla\Phi_e$	0	0

alyst layers where electrochemical reactions take place. The S_k and S_Φ terms are therefore related to the transfer current between the solid matrix and the membrane phase inside each of the catalyst layers. These transfer currents at anode and cathode can be expressed as follows[4]

$$j_a = aj_{0,a}^{ref}\left(\frac{X_{H_2}}{X_{H_2,ref}}\right)^{1/2}\left(\frac{\alpha_a + \alpha_c}{RT}\cdot F\cdot\eta\right) \quad [13]$$

$$j_c = -aj_{0,c}^{ref}\left(\frac{X_{O_2}}{X_{O_2,ref}}\right)\exp\left(-\frac{\alpha_c F}{RT}\cdot\eta\right) \quad [14]$$

The above kinetics expressions are derived from the general Butler-Volmer equation based on the facts that the anode exhibits fast electrokinetics and hence a low surface overpotential to justify a linear kinetic rate equation, and that the cathode has relatively slow kinetics to be adequately described by the Tafel equation. In Eq. 13 and 14, the surface overpotential, $\eta(x, y)$, is defined as

$$\eta(x, y) = \Phi_s - \Phi_e - V_{oc} \quad [15]$$

where Φ_s and Φ_e stand for the potentials of the electronically conductive solid matrix and electrolyte, respectively, at the electrode/electrolyte interface. V_{oc} is the reference open-circuit potential of an electrode. It is equal to zero on the anode but is a function of temperature on the cathode,[24] namely

$$V_{oc,+} = 0.0025T + 0.2329 \quad [16]$$

where T is in kelvin and V_{oc} is in volts. Notice that V_{oc} is not the true open-circuit potential of an electrode, which would then depend upon reactant concentrations according to the Nernst equation. Instead, V_{oc} is only the constant part of the open-circuit potential. Its concentration-dependent part in logarithmic form can then be moved out of the exponent in the Butler-Volmer equation and now becomes the concentration terms in front of the exponent in Eq. 13 and 14, respectively. Equation 13, which is a rewritten form of the Nernst equation, precisely describes the effect of decreasing transfer current under hydrogen dilution. Based on the experimental data of Parthasarathy *et al.*,[24] the dependence of the cathodic exchange current density on temperature can be fitted as

$$\frac{i_0(T)}{i_0(353\ K)} = \exp[0.014189\ (T - 353)] \quad [17]$$

Under the assumption of a perfectly conductive solid matrix for electrodes and catalyst layers, Φ_s is equal to zero on the anode side at the anodic current collector and to the cell voltage on the cathode side at the cathodic current collector. Thus, the surface overpotential given by Eq. 15 is only dependent on the membrane phase potential, which is to be solved from Eq. 6.

The species diffusivity, D_k, varies in different subregions of the PEMFC depending on the specific physical phase of component k. In flow channels and porous electrodes, species k exists in the gaseous phase, and thus the diffusion coefficient takes the value in gas, whereas species *k* is dissolved in the membrane phase within the catalyst layers and the membrane, and thus takes the value corresponding to dissolved species, which is usually a few orders of magnitude lower than that in gas (see Table II). In addition, the diffusion coefficient is a function of temperature and pressure,[25] *i.e.*

$$D(T) = D_0\left(\frac{T}{T_o}\right)^{3/2}\left(\frac{p_o}{p}\right) \quad [18]$$

The proton conductivity in the membrane phase has been correlated by Springer *et al.*[7] as

$$\sigma_e(T) = 100\ \exp\left[1268\left(\frac{1}{303} - \frac{1}{T}\right)\right](0.005139\lambda - 0.00326)$$

in S/cm [19]

where the water content in the membrane, λ, depends on the water activity, *a*, according to the following fit of the experimental data

$$\lambda = \begin{cases} 0.043 + 17.18a - 39.85a^2 + 36.0a^3 & \text{for } 0 < a \le 1 \\ 14 + 1.4(a - 1) & \text{for } 1 \le a \le 3 \end{cases} \quad [20]$$

The water activity is in turn calculated by

$$a = \frac{X_{H_2O}p}{p^{sat}} \quad [21]$$

where the saturation pressure of water vapor can be computed from Springer *et al.*[7]

$$\log_{10} p_{sat} = -2.1794 + 0.02953\ (T - 273.15) - 9.1837 \times 10^{-5}\ (T - 273.15)^2 + 1.4454 \times 10^{-7}\ (T - 273.15)^3 \quad [22]$$

The above calculated saturation pressure is in bars. Apparently, the water mole fraction X_{H2O}, water activity, and water content all vary spatially in the membrane layer, and thus the membrane conductivity σ_e is a variable.

For this multicomponent system, the general species transport equation given in Eq. 5 is applied to solve for mole fractions of

S0013-4651(00)08-104-0 CCC: $7.00

Table II. Physical parameters and properties at 353 K.

Quantity	Value
Gas channel length, L	7.112 cm
Gas channel width	0.0762 cm
Backing layer width	0.0254 cm
Catalyst layer width	0.00287 cm
Membrane width	0.023 cm
Fixed charge concentration, c_f	1.2×10^{-3} mol/cm^3
Oxygen diffusivity in gas	5.2197×10^{-2} cm^2/s
Hydrogen diffusivity in gas	2.63×10^{-2} cm^2/s
Dissolved oxygen diffusivity in active layer and membrane	2.0×10^{-4} cm^2/s
Dissolved hydrogen diffusivity in active layer and membrane	2.59×10^{-6} cm^2/s
Faraday constant, F	96487 C/mol
Hydraulic permeability of membrane, k_p	1.8×10^{-14} cm^2
Permeability of backing layer, K	1.76×10^{-7} cm^2
Electrokinetic permeability, k_Φ	7.18×10^{-16} cm^2
Universal gas constant, R	8.314 J/mol K
Fixed site charge, z_f	-1
Cathodic transfer coefficient α_c	2
Anodic transfer coefficient, α_a	2
Backing layer porosity, ϵ	0.4
Membrane water porosity, ϵ_m	0.28
Volume fraction membrane in catalyst layer, ϵ_{mc}	0.4
Inlet nitrogen-oxygen mole ration, X_{N_2}/X_{O_2}	0.79/0.21
Air-side inlet pressure/fuel-side inlet pressure	5/3 atm
O_2 stoichiometric flow ratio, ζ_+	3.0
H_2 stoichiometric flow ratio, ζ_-	2.8
Relative humidity of inlet air/fuel (anode/cathode)	100/0%
Reference exchange current density × area of anode, $aj_{0,a}^{ref}$	5.0×10^2 A/cm^3
Reference exchange current density × area of cathode, $aj_{0,c}^{ref}$	1.0×10^{-4} A/cm^3
Total mole concentration at the anode side, c_{tota}	66.817×10^{-6} mol/cm^3
Total mole concentration at the cathode side, c_{totc}	17.808×10^{-6} mol/cm^3

hydrogen, oxygen, and water vapor. The mole fraction of nitrogen is then obtained by the following constraint

$$X_{N2} = 1 - X_{H2} - X_{H2O} \quad \text{on the anode side} \qquad [23a]$$

$$X_{N2} = 1 - X_{O2} - X_{H2O} \quad \text{on the cathode side} \qquad [23b]$$

Once the electrolyte phase potential is determined in the membrane, the local current density along the axial direction can be calculated as follows

$$I(y) = -\sigma_e^{eff} \left.\frac{\partial \Phi_e}{\partial x}\right|_{x=\text{I.F.}} \qquad [24]$$

where I.F. means the interface between the membrane and cathode catalyst layer. The average current density is then determined by

$$I_{avg} = \frac{1}{L}\int_0^L I(y)\, dy \qquad [25]$$

where L is the cell length.

Boundary conditions.—Equations 3-6 form a complete set of governing equations for $(m + 5)$ unknowns, where m is the physical dimension of the problem: **u,** p, X_{H2}, X_{O2}, X_{H2O}, and Φ_e. Their boundary conditions are required only at the external surfaces of the computational domain due to the single-domain formulation used. These are no-flux conditions everywhere except for the inlets and outlets of the flow channels. At the fuel and oxidant inlets, the following conditions are prescribed

$$u_{in,anode} = U^0, \quad u_{in,anode} = U_+^0 \qquad [26]$$

$$X_{H2,anode} = X_{H2,-}, X_{O2,cathode} = X_{O2,+}, X_{H2O,anode} = X_{H2O,-}, X_{H2O,cathode} = X_{H2,+} \qquad [27]$$

The inlet velocities of fuel and oxidant can also be expressed by their respective stoichiometric flow ratios, *i.e.*, ζ_- and ζ_+ at 1 A/cm^2. At the outlets, both channels are assumed sufficiently long that velocity and species concentration fields are fully developed. The boundary condition for the electrolyte phase potential is no-flux everywhere along the boundaries of the computational domain.

Numerical procedures.—The conservation equations (Eq. 3-6) were discretized using a finite-volume method[26] and solved using a general-purpose CFD code. Details of the numerical solution procedure and the code have been given in previous work.[16,18] Worthy of mention here is that although some species are practically nonexisting in certain regions of a fuel cell, the species transport equation can still be applied throughout the entire computational domain by using the large source term technique originally proposed by Voller.[27] For example, there is virtually no hydrogen in the cathode catalyst layer, gas-diffusion cathode, and cathode gas channel. Therefore, in these subregions, a sufficiently large source term is assigned to the hydrogen transport equation, which effectively freezes the hydrogen mole fraction at zero.

The jump condition in the mole fraction across the catalyst/backing layer interface as expressed by Eq. 9 can be numerically treated by a standard interfacial resistance approach which is detailed in the Appendix.

Stringent numerical tests were performed to ensure that the solutions were independent of the grid size. A 35×90 mesh provides sufficient spatial resolution. The coupled set of equations was solved simultaneously, and the solution was considered to be convergent when the relative error in each field between two consecutive iterations was less than 10^{-5}. A typical simulation involving approximately 22,000 unknowns required about 10 min of central processing unit time on a 600 MHz PC.

Results and Discussion

Experimental validation.—To validate the numerical model presented in the preceding section, comparisons were made to the experimental data of Ticianelli *et al.*[23] for a single cell operated at two different temperatures. The parameters used in the following

S0013-4651(00)08-104-0 CCC: $7.00

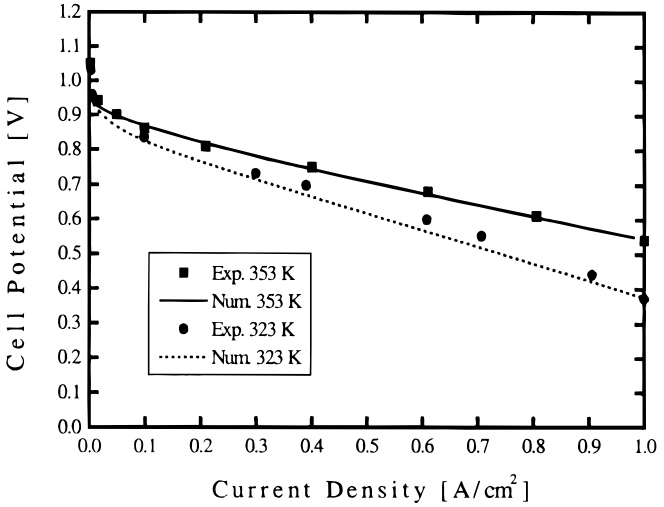

Figure 2. Comparison of predicted and measured cell polarization curves at two operating temperatures. The experimental data were adapted from Ticianelli *et al.*[23]

simulations were taken from Bernardi and Verbrugge[6] and are summarized in Table II.

Figure 2 compares the computed polarization curves with the measured ones. The calculated curves show good agreement with the experimental data for both temperatures. The product of the specific interfacial area and the exchange current density for the anodic reaction used in these simulations is so large that the predicted surface overpotential prevailing in the anode catalyst layer is practically negligible, which is in accordance with the experimental measurement.

While no data of velocity and concentration fields were provided in the experiments of Ticianelli *et al.*,[23] these detailed results can also be generated from the present model to shed light on the internal operation of the fuel cell. Figure 3 shows the predicted flow field inside the entire cell and the water vapor and oxygen mole fraction

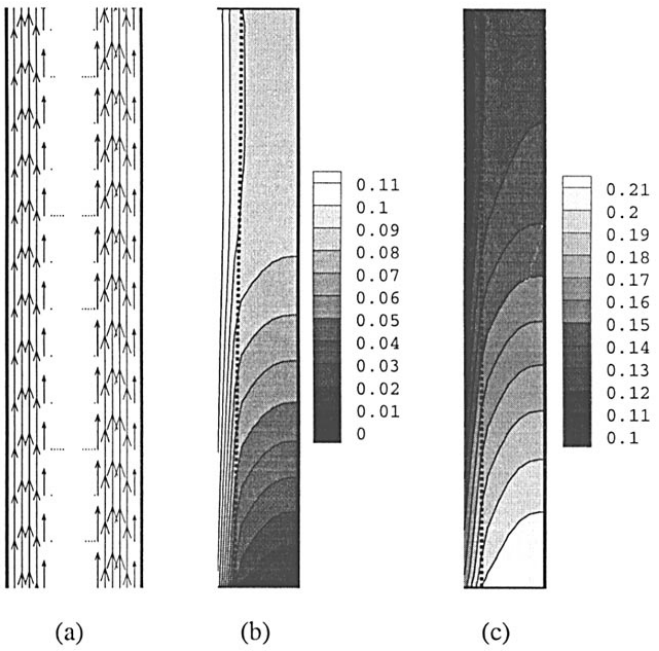

Figure 3. (a) Computed velocity profiles in anode and cathode flow channels, (b) water vapor mole fraction, and (c) oxygen mole fraction in the cathode gas diffuser and flow channel for $V_{cell} = 0.6$ V, $X^0_{H2O,+} = 0$, and $T = 353$ K. The left boundary in (b) and (c) is the interface between catalyst layer and gas-diffusion cathode.

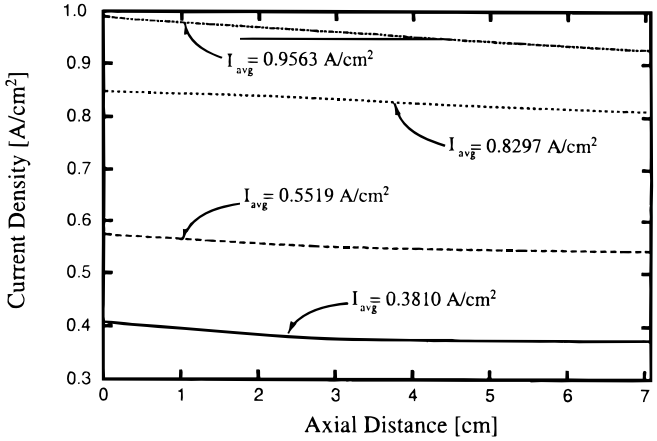

Figure 4. Local current density distributions in the axial distance (*y* direction) for $X^0_{H2O,+} = 0$ and $T = 353$ K.

fields within the porous cathode and its adjacent flow channel for the experimental fuel cell at 353 K. The velocity exhibits parabolic profiles in both anode and cathode gas channels and reduces essentially to zero in the regions of porous structure. The water vapor mole fraction increases along the cathode gas channel while the mole fraction of oxygen decreases, due to the electrochemical reaction within the cathode catalyst layer, where oxygen is reduced by protons migrating through the membrane from the anode side to produce water. A detailed oxygen mole fraction profile along the *x* direction in the midlength plane (*i.e.*, $y = L/2$) of the cathode is displayed in Fig. A-2 of the Appendix, demonstrating that the jump condition in oxygen concentration at the interface between the catalyst and backing layers is successfully captured by the present computer model.

Figure 4 displays the local current density distributions at various average current densities along the axial direction of fuel cells. The current density distributions are uniform at all cell average current densities, probably due to the small cell and high stoichiometric flow ratios employed in these experiments.

In the present model, it is assumed that water only exists in the vapor state. However, if the electrochemical reaction rate is sufficiently high, the amount of water produced is condensed into the liquid phase. In this situation, two-phase flow and transport may have to be considered. Figure 5 displays water vapor mole fraction profiles along the interface between the catalyst layer and gas diffuser on the cathode side where there is the highest content of water vapor. When the cell current density is higher than about 0.6 A/cm^2, the water vapor mole fraction along the catalyst layer/gas diffuser interface

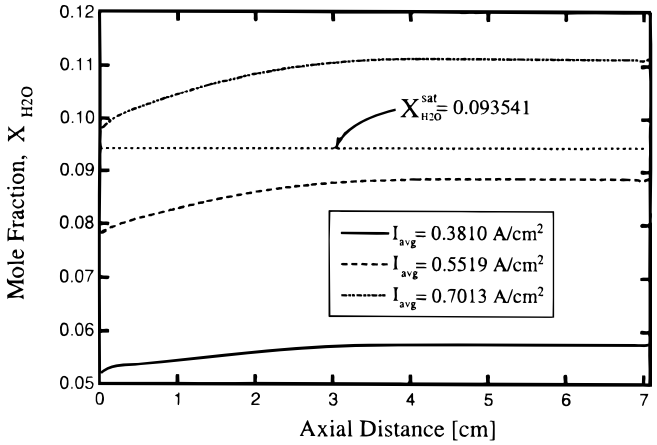

Figure 5. Water vapor mole fraction profiles along the interface between the cathode catalyst layer and gas diffuser for $X^0_{H2O,+} = 0$ and $T = 353$ K.

S0013-4651(00)08-104-0 CCC: $7.00

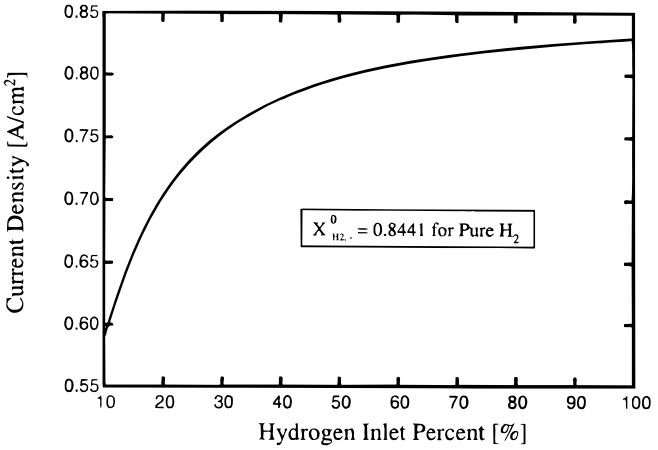

Figure 6. Hydrogen dilution effect on the cell average current density for $X^0_{H2O,+} = 0$, $V_{cell} = 0.6$ V, and $T = 353$ K.

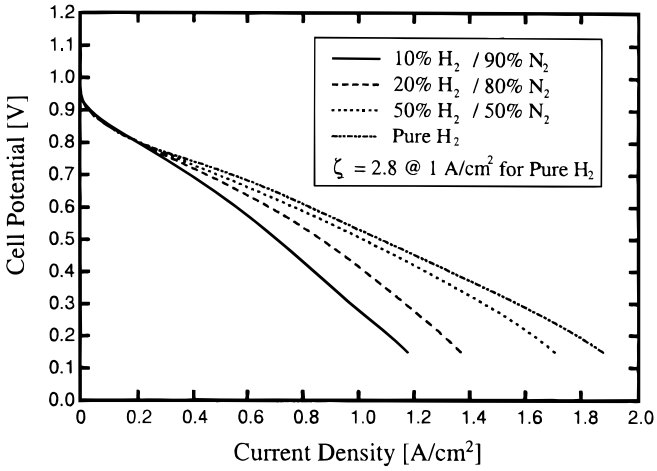

Figure 7. Effect of the inlet hydrogen mole fraction on cell polarization curves for $X^0_{H2O,+} = 0$.

already exceeds the saturated level, *i.e.*, $X^{sat}_{H2O} = 0.093541$ at a pressure of 5 atm and a cell temperature of 353 K. Hence, it suggests that the two-phase flow regime already starts at intermediate current densities. Nonetheless, a single-phase analysis such as the present model and all existing models[6-11] still provides a good first approximation of cell performance for current densities above 0.6 A/cm^2. This is true because the water distribution affects the electrochemical process and oxygen transport in the air cathode primarily in two ways.

First, the presence of liquid water affects the water content in the membrane and thus slightly alters its ionic conductivity. More important, liquid water present in the gas diffusion cathode hampers oxygen transport to the catalyst layer. However, recent two-phase calculations[15,28] indicated that there is only 5% of the liquid water saturation at current densities as high as 1.5 A/cm^2, making the effect of liquid water existence on the oxygen transport likely minimal. For these reasons, the present single-phase analysis is still applied to predict cell performance for current densities greater than 0.6 A/cm^2 in the following without consideration given to the water distribution. Rigorous two-phase analysis, however, is the subject of future work.

Hydrogen dilution effects.—When reformate gas is used as the anode feed, the hydrogen mole fraction at the anode inlet is significantly lower than that in the pure hydrogen condition (*i.e.*, hydrogen plus water vapor only). Consequently, hydrogen dilution has a strong effect on cell performance. A series of simulations for different hydrogen inlet fractions at the anode were carried out to illustrate this effect. In all these simulations, the stoichiometric flow ratios of fuel and oxidant are fixed at 2.8 and 3.0 at 1 A/cm^2, respectively. Figure 6 and 7 show that the cell current density at a cell voltage of 0.6 V decreases significantly as the inlet hydrogen content is lowered, particularly in the range below 50%. The cell polarization curves under pure and hydrogen dilution conditions are displayed in Fig. 7, showing qualitatively good agreement with the most recent experiments of Rockward *et al.*[1] A quantitative comparison is not possible due to a lack of specific information about the experiments that were only reported in a meeting abstract.[1]

Figure 8 shows predicted profiles of the membrane phase potential across the anode catalyst layer, the membrane, and the cathode catalyst layer at various axial locations for $V_{cell} = 0.85$ and 0.6 V. The membrane phase potential is in reference to the anode solid potential of zero. For pure hydrogen, nearly zero overpotential is predicted within the anode catalyst layer, indicating that the hydrogen oxidation kinetics on the anode is much faster than the cathode reaction. Furthermore, the membrane phase potential profile remains similar at different axial locations. However, in the presence of large hydrogen dilution, the overpotential for the hydrogen oxidation within the anode catalyst layer significantly increases as the hydrogen mole fraction at the reaction surface is drastically reduced. This is easily explained by Eq. 9 where the transfer current is proportional to the square root of the hydrogen mole fraction. At low operating current densities (*e.g.*, < 0.2 A/cm^2), hydrogen is not being depleted in the catalyst layer or along the flow channel (since H_2 stoichiometry is 2.4 at 1 A/cm^2). Hence, the overpotential changes negligibly for hydrogen bulk concentrations ranging from one hundred to ten percents. This can be seen clearly from Fig. 8 left side. However, at large current densities, the anode gas is progressively depleted of hydrogen downstream along the gas channel as it is consumed by the electrochemical reaction, and thus the overpotential required to sustain a particular current density becomes substantially larger. There are also appreciable differences in the membrane phase potential

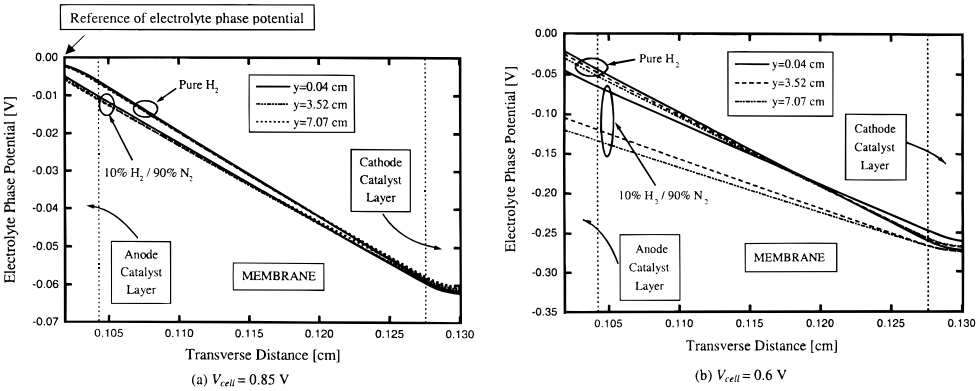

Figure 8. Phase potential distributions in the transverse direction (x direction) for $X^0_{H2O,+} = 0$, $T = 353$ K, and $\zeta_- = 2.8$ at 1 A/cm^2 for pure H_2.

S0013-4651(00)08-104-0 CCC: $7.00

profile at various locations along the channel, as seen from Fig. 8 right. A limiting current density may occur when hydrogen is completely depleted at the reaction surface, thus leading to an infinitely large anode polarization loss. The prediction that there is no performance change under hydrogen dilution for low current densities disagrees with the experimental observations of Rockward *et al.*,[1] indicating possible contributors other than the mass-transfer limitation modeled here.

Figure 9 shows the two-dimensional contours of hydrogen mole fraction in the anode gas channel and porous electrode under V_{cell} = 0.6 V for 10% hydrogen dilution and for no dilution. Under the hydrogen dilution condition, the hydrogen mole fraction decreases along the flow channel as well as across the porous anode. These trends are more apparent from Fig. 10, which displays the hydrogen mole fraction profiles at several important boundaries. The down-the-channel effect becomes particularly significant in the high fuel utilization conditions that are needed for the highest possible fuel efficiency. However, this effect can be alleviated by using large fuel flow rates, *i.e.*, at the expense of fuel utilization. For example, the down-the-channel effect is not significant in the case displayed in Fig. 10. The substantial drop of H_2 mole fraction across the anode is caused by diffusion of hydrogen from the anode stream to the reaction surface, a limiting step for the cell current density in this case. On the contrary, the hydrogen supply from the fuel stream to the reaction surface appears adequate in the case of no dilution, as seen in Fig. 9b.

The above simulations provide a good illustration of the capabilities of the present model. Although the results for hydrogen dilution effects are realistic, more detailed analyses and parametric studies are desirable to fully investigate hydrogen dilution and high fuel utilization effects. These studies are the subject of work in the near future.

The present CFD model can also simulate the transient response of a fuel cell to dynamically varying operating conditions. Figure 11 shows a preliminary example in which the cell voltage undergoes a step change from 0.6 to 0.55 V. The figure shows that the cell current density abruptly adjusts to a new value because the charge-transfer reaction and membrane potential equation respond instantaneously. Subsequently, the concentration fields begin to evolve, gradually reducing the cell current density to the steady-state value corresponding to V_{cell} = 0.55 V. This transient simulation demonstrates the interesting phenomenon of current overshoot as well as the fuel cell transient response time of the order of a couple of seconds. Detailed transient results are reported in a separate publication due to the space limitation of this paper.

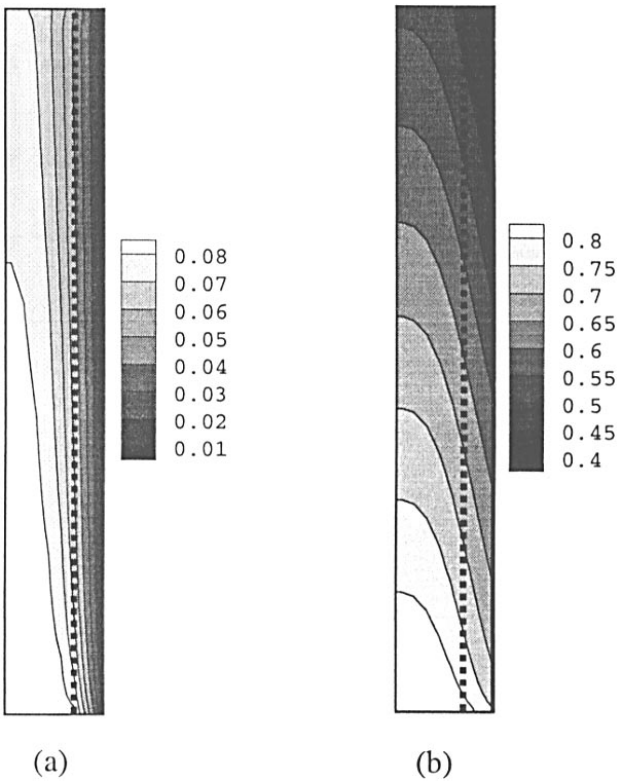

Figure 9. Hydrogen mole fraction distributions in the anode flow channel and gas diffusion electrode for $X^0_{H2O,+}$ = 0, V_{cell} = 0.6 V, T = 353 K, and ζ_- = 2.8 at 1 A/cm^2. (a) 10% hydrogen $X^0_{H2,-}$ = 0.08441) and (b) pure hydrogen $X^0_{H2,-}$ = 0.8441).

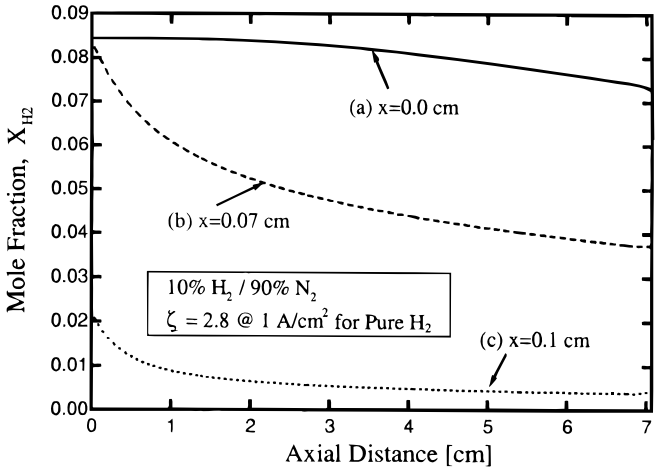

Figure 10. Hydrogen mole fraction profiles at (a) the flow channel wall, (b) the interface between the anode flow channel and gas-diffusion electrode, and (c) the interface between the gas-diffusion anode and catalyst layer for $X^0_{H2O,+}$ = 0, V_{cell} = 0.6 V, and T = 353 K.

Conclusion

A single-domain formulation was developed to comprehensively describe electrochemical kinetics, current distribution, hydrodynamics, and multicomponent transport in hydrogen PEMFCs. A finite-volume-based CFD technique was successfully adapted to simulate multidimensional behaviors of the fuel cell. The CFD model was able to predict not only the experimental polarization curves of Ticianelli *et al.*[23] but also the detailed reactant and product distributions inside the cell. In addition, the CFD model was used to understand the hydrogen dilution effect when the reformate gas is used as the anode feed. Hydrogen dilution leads to a much lower cell current density that is limited by the diffusive transport of hydrogen to the reaction site. Efforts are presently underway to undertake three-dimensional and two-phase analyses of PEMFCs.

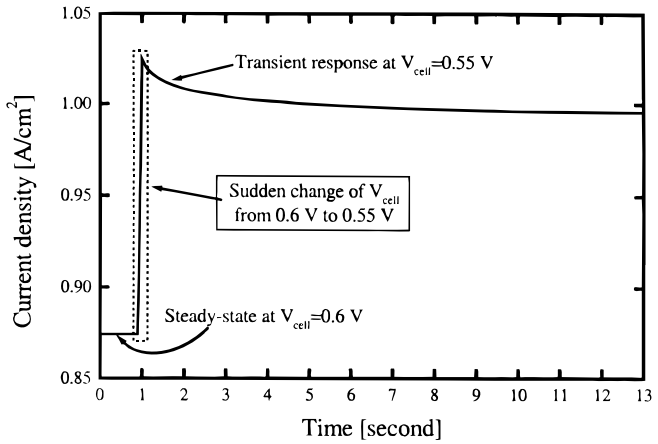

Figure 11. Transient response of current density from V_{cell} = 0.6 to 0.55 V for $X^0_{H2,+}$ = 0, T = 353 K, and ζ_- = 2.8 at 1 A/cm^2 for pure H_2.

S0013-4651(00)08-104-0 CCC: $7.00

Acknowledgments

This work was partially supported by Sandia National Laboratories under contract no. BF-6597. Sandia is a multiprogram laboratory operated by Sandia Corporation, a Lockheed Martin Company, for the United States Department of Energy under contract DE-AC04-94AL85000. The work is also supported by NSF under grant no. DUE-9979579.

The Pennsylvania State University assisted in meeting the publication costs of this article.

Appendix

Numerical Treatment of Concentration Discontinuity at Catalyst Layer/Backing Layer Interface

Consider the concentration profile in the two control volumes surrounding the interface between the catalyst and backing layers, as shown in Fig. A-1. Following Henry's law, the concentration undergoes a discontinuity across the interface because it represents the value in the membrane phase within the catalyst layer but stands for the value in the gas phase within the backing layer. In Fig. A-1, subscripts in capital letters denote central nodal points of control volumes, whereas the corresponding subscript in lowercase represents the face of the control volume.

The total diffusion flux across the interface can be written as follows

$$J = D_g \frac{(c_P - c_{w-})}{(\delta x)_{w-}} = D_e \frac{(c_{w+} - c_W)}{(\delta x)_{w+}} = h_{int}(c_{w-} - c_{w+}) \quad [A\text{-}1]$$

where h_{int} is an effective interfacial mass-transfer coefficient introduced to numerically model the concentration discontinuity. Its value can thus be determined by

$$h_{int} = \frac{J}{c_{w-} - c_{w+}} = \frac{J}{c_{w-} - H'c_{w-}} = \frac{J}{(1 - H')c_{w-}} \quad [A\text{-}2]$$

Since

$$c_{w-} = c_P - \frac{(\delta x)_{w-} J}{D_g} \quad [A\text{-}3]$$

Equation A-2 can be rewritten as

$$h_{int} = \frac{J}{(1 - H')\left[c_P - \frac{(\delta x)c_{w-}J}{D_g}\right]} \quad [A\text{-}4]$$

The overall conductivity at the interface for use in a CFD model is traditionally defined as

$$J = \frac{k_{int}}{(\delta x)_W}(c_P - c_W) \quad [A\text{-}5]$$

Therefore, one obtains the following from Eq. A-1

$$\frac{(\delta x)_W}{k_{int}} = \frac{(\delta x)_{w+}}{D_e} + \frac{(\delta x)_{w-}}{D_g} + \frac{1}{h_{int}} \quad [A\text{-}6]$$

Substituting Eq. A-4 into A-6 yields

$$k_{int} = \left[\frac{f_w}{D_e} + \frac{(1 - f_w)}{D_g} + (1 - H')\cdot\left\{\frac{c_P}{J(\delta x)_W} - \frac{(1 - f_w)}{D_g}\right\}\right]^{-1} \quad [A\text{-}7]$$

where

$$f_w = \frac{(\delta x)_{w+}}{(\delta x)_W} \quad [A\text{-}8]$$

Equation A-7 can be simply implemented in a CFD code to simulate the jump condition at the catalyst/backing interface. Note that if $H' = 1$ (*i.e.*, in the absence of a jump condition), the last term in Eq. A-7 vanishes and Eq. A-7 identically reduces to the conventional geometrical mean formula. However, if $H' < 1$, an additional resistance arises at the interface, effectively simulating the jump condition in the concentration. Note that Eq. A-7 must be iterated to update the flux, *J;* however, calculations indicated that this iteration is quickly convergent.

A representative oxygen mole fraction profile in the midlength plane (*i.e.*, $y = L/2$) across the entire air cathode, including the membrane, catalyst layer, and backing layer, is shown in Fig. A-2. The cell operating conditions are identical to those corresponding to Fig. 3. The oxygen mole fraction starts from about 0.17 at the outer face of the backing layer due to gradual depletion along the flow channel, further reduces to approximately 0.14 in the gas phase at the catalyst/backing interface due to mass-transport resistance within the backing layer, and undergoes a discontinuous drop at the interface to about 0.02, a value for the membrane phase in accordance with Henry's law. Subsequently, all oxygen in the membrane phase is consumed by the oxygen reduction reaction, which occurs within a short distance from the catalyst/backing interface. The general trends are consistent with those predicted by the one-dimensional model of Bernardi and Verbrugge.[5]

List of Symbols

a effective catalyst area per unit volume, cm^2/cm^3
A superficial electrode area, cm^2

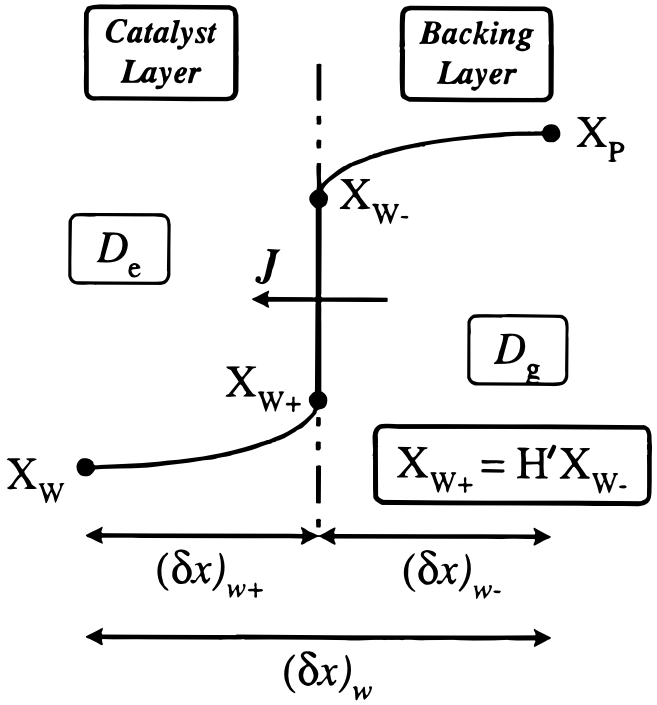

Figure A-1. Schematic of concentration profiles in the two control volumes in the vicinity of the interface between the catalyst layer and the backing layer in the cathode.

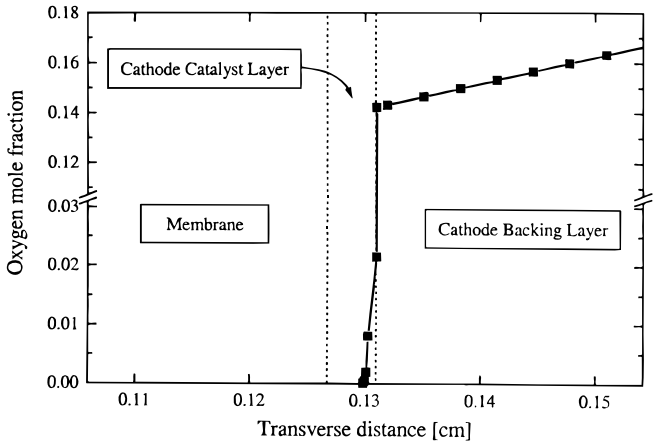

Figure A-2. Oxygen mole fraction profile across the membrane, catalyst layer, and backing layer on the cathode side at $y = L/2$. Cell conditions are identical to those in Fig. 3.

S0013-4651(00)08-104-0 CCC: $7.00

c molar concentration, mol/cm^3
D mass diffusivity of species, cm^2/s
I current density, A/cm^2
j transfer current, A/cm^3
p pressure, Pa
R gas constant, 8.314 J/mol K
S source term in transport equations
t time, s
T temperature, K
u velocity vector, cm/s
U inlet velocity, cm/s
V cell potential, V
X mole fraction of species

Greek

λ membrane water content, H_2O/mol SO_3^-
Φ phase potential, V
η overpotential, V
μ viscosity, kg/m s
ν kinematic viscosity, cm^2/s
ϑ volumetric flow rate, cm^3/s
ρ density, kg/cm^3
σ ionic conductivity, S/cm
ζ stoichiometric flow ratio, Eq. 1

Superscripts

o gas channel inlet value
eff effective value
sat saturation value

Subscripts

a anode
c cathode
e electrolyte
k species
m membrane
oc open circuit
ref reference value
s solid phase of electrode
u momentum equation
Φ potential equation
$+$ cathode
$-$ anode

References

1. T. Rockward, T. Zawodzinski, J. Bauman, F. Uribe, J. Valerio, T. Springer, and S. Gottesfeld, Abstract 566, The Electrochemical Society Meeting Abstracts, Vol. 99-1, Seattle, WA, May 2-6, 1999.
2. J. K. Hong, L. A. Zook, M. Inbody, J. Tafoya, and N. E. Vanderborgh, Abstract 570, The Electrochemical Society Meeting Abstracts, Vol. 99-1, Seattle, WA, May 2-6, 1999.
3. K. B. Prater, *J. Power Sources*, **51,** 129 (1994).
4. S. Gottesfeld, in *Advances in Electrochemical Science and Engineering*, C. Tobias, Editor, Vol. 5, p. 195, John Wiley & Sons, New York (1997).
5. D. M. Bernardi and M. W. Verbrugge, *AIChE J.*, **37,** 1151 (1991).
6. D. M. Bernardi, and M. W. Verbrugge, J. Electrochem. Soc., **139,** 2477 (1992).
7. T. E. Springer, T. A. Zawodinski, and S. Gottesfeld, *J. Electrochem. Soc.*, **136,** 2334 (1991).
8. T. E. Springer, M. S. Wilson, and S. Gottesfeld, *J. Electrochem. Soc.*, **140,** 3513 (1993).
9. T. F. Fuller and J. Newman, *J. Electrochem. Soc*, **140,** 1218 (1993).
10. T. V. Nguyen and R. E. White, *J. Electrochem. Soc.*, **140,** 2178 (1993).
11. V. Gurau, H. Liu, and S. Kakac, *AIChE J.*, **44,** 2410 (1998).
12. J. S. Yi and T. V. Nguyen, *J. Electrochem. Soc.*, **145,** 1149 (1998).
13. J. S. Yi and T. V. Nguyen, *J. Electrochem. Soc.*, **146,** 38 (1999).
14. T. V. Nguyen, Paper 880 presented at The Electrochemical Society Meeting, Seattle, WA, May 2-6, 1999.
15. C. Y. Wang, Z. H. Wang, and Y. Pan, in *Proceedings of ASME Heat Transfer Division-1999*, HTD-Vol, 364-1, ASME, New York, p. 351 (1999).
16. W. B. Gu, C. Y. Wang, and B. Y. Liaw, *J. Electrochem Soc.*, **144,** 2053 (1997).
17. W. B. Gu, C. Y. Wang, and B.Y. Liaw, *J. Power Sources*, **75/1,** 154 (1998).
18. W. B. Gu, C. Y. Wang, and B. Y. Liaw, *J. Electrochem Soc.*, **145,** 3418 (1998).
19. C. Y. Wang, W. B. Gu, and B.Y. Liaw, *J. Electrochem. Soc.*, **145,** 3407 (1998).
20. C. Y. Wang, W. B. Gu, R. Cullion, and B. Thomas, in *Proceedings of IMECE99*, ASME, New York (1999).
21. W. B. Gu, C. Y. Wang, S. Li, M. M. Geng and B. Y. Liaw, *Electrochim. Acta*, **44,** 4525 (1999).
22. W. B. Gu, C. Y. Wang, J. Weidner, R. Jungst, and G. Nagasubramanian, *J. Electrochem. Soc.*, **147**, 427 (2000).
23. E. A. Ticianelli, C. R. Derouin, and S. Srinivasan, *J. Electroanal. Chem.*, **251,** 275 (1988).
24. A. Parthasarathy, S. Srinivasan, and A. J. Appleby, *J. Electrochem Soc.*, **139,** 2530 (1992).
25. R. B. Bird, W. E. Stewart, and E. N. Lightfoot, *Transport Phenomena*, John Wiley & Sons, New York (1960).
26. S. V. Patankar, *Numerical Heat Transfer and Fluid Flow*, Hemisphere, New York (1980).
27. V. R. Voller, *Numer. Heat Transfer, Part B*, **17,** 155 (1990).
28. T. V. Nguyen, in *Tutorials in Electrochemical-Engineering Mathematical Modeling*, R. F. Savinell, J. M. Fenton, A. West, S. L. Scanlon, J. Weidner, Editors, PV 99-14, p. 222, The Electrochemical Society Proceedings Series, Pennington, NJ (199).